Three-Body Dissociative Charge Exchange Dynamics of *sym*-Triazine†

John D. Savee, Jennifer E. Mann, and Robert E. Continetti*

Department of Chemistry and Biochemistry, University of California at San Diego, 9500 Gilman Drive, La Jolla, California 92093-0340

Received: November 25, 2008; Revised Manuscript Received: January 27, 2009

Translational spectroscopy and coincidence detection techniques have been employed to observe the three-body dissociation dynamics resulting from charge exchange between a fast molecular beam of the *sym*-triazine cation ($C_3N_3H_3^+$) and cesium. The energetics and momentum correlation between the three hydrogen cyanide products suggest that dissociation proceeds via two mechanisms that reflect the initial excited states in which *sym*-triazine is produced. Monte Carlo simulations support a stepwise mechanism resulting from initial excitation into the 3s Rydberg state. Excitation into the valence $\pi^* \leftarrow$ n manifold was found to proceed via a near-symmetric concerted mechanism, in agreement with recent theoretical studies on the dissociation of *sym*-triazine.

1. Introduction

In many nonequilibrium environments (e.g., biological systems, the atmosphere, and combustion) molecular dissociation plays an important role in the underlying chemistry. In some cases molecules can be excited with enough energy (e.g., via dissociative recombination or photolysis) to break multiple bonds, resulting in three or more dissociation products.[1,2] Obtaining a full understanding of these higher order processes poses a significant challenge to both experimentalists and theoreticians; a full description of the complex kinematics associated with *n*-body ($n \geq 3$) dissociation typically requires direct observation of multiple fragments in coincidence, and the dissociation of highly excited molecules is often the result of complex nonadiabatic interactions which can be difficult to predict theoretically.

In two recent publications we presented an investigation into the three-body dissociation of *sym*-triazine (Tz) to hydrogen cyanide products upon charge exchange (CE) of the *sym*-triazine radical cation (Tz^+) with cesium (eq 1).[3,4]

$$C_3N_3H_3^+ + Cs \rightarrow C_3N_3H_3^* + Cs^+ \xrightarrow{-Cs^+} 3HCN \quad (1)$$

Charge exchange between a fast cation beam and an alkali electron donor has long been known to be an effective method for producing excited neutral molecules that can be probed by using translational spectroscopy and coincidence measurements, and its utility has been confirmed in recent studies on H_3 and CH_5.[5−13] Through the use of these coincidence detection techniques and high-level ab initio calculations it was shown that two initial excited electronic states of Tz were populated, and, after nonadiabatic coupling to the ground electronic state, give rise to unique dissociation mechanisms consistent with the topologies of the initial potential energy surfaces (PESs).[3,4] Like many other molecules that exhibit three-body dissociation, Tz has a rich history of mechanistic debate.[2,14−19] In the present experiment Tz was directly observed to dissociate by both stepwise and concerted mechanisms, which is of interest not only in light of past discussion on Tz but also because this marks the first observation of these two distinct mechanisms proceeding from a single molecule. Excitation into the conical intersection of two electronic states comprising the 3s Rydberg ($R_s \leftarrow$ n) manifold was observed to give rise to a stepwise dissociation mechanism, whereas excitation into the glancing intersection of the four electronic states in the $\pi^* \leftarrow$ n manifold resulted in a near-symmetric concerted dissociation.[3,4] Although it will be discussed in more detail later, Figure 1 presents a simple energy level diagram that illustrates the calculated locations of relevant electronic manifolds for Tz and the range over which the two dissociation mechanisms were observed in refs 3 and 4, along with the experimentally determined location of excited electronic states of Tz from photoexcitation studies as reported in an azabenzene review by Innes et al.[20]

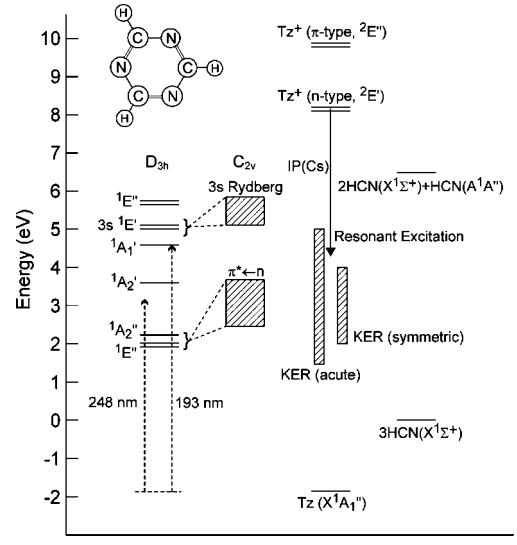

Figure 1. Energy level diagram for three-body dissociation of Tz. Locations of D_{3h} excited states are vertical measurements from the neutral ground state as reported in the azabenzene review by Innes et al.[20] The hatched C_{2v} regions are between minima for the lowest and highest states (including triplets) contributing to the $\pi^* \leftarrow$ n and 3s Rydberg manifolds as reported by Mozhayskiy et al.[4]

† Part of the "George C. Schatz Festschrift".

* E-mail: rcontinetti@ucsd.edu.

10.1021/jp810365f CCC: $40.75
Published on Web 03/13/2009

Coincidence detection of the HCN products provides a considerable advantage over the time-of-flight (TOF) methods used in previous translational spectroscopy studies—coincidence measurements allow full kinematic descriptions of the dissociation process on a per-event basis, whereas the equal-mass HCN products limit the dynamical information obtainable by TOF methods to ensemble averages. In two previous translational spectroscopy studies carried out by Ondrey et al. and Gejo et al., the three-body dissociation of neutral Tz was initiated by using 248 and 193 nm photons which are believed to respectively excite Tz into the $\pi^* \leftarrow$ n and $\pi^* \leftarrow \pi$ manifolds.[14,15] In the latter of these studies, Gejo et al. concluded that dissociation was proceeding via an asynchronous concerted mechanism (stepwise, but retaining angular correlation in the products). Several other notable experiments aimed at characterizing the internal energy of HCN products upon photolysis of Tz have shown that a large fraction of the photon energy is deposited as rotational and vibrational excitation in HCN, with a high propensity for exciting the HCN bending mode in particular.[21−23]

Ensuing theoretical works have disputed the mechanism proposed by Gejo et al., and will be briefly reviewed here. In an ab initio investigation into critical points for concerted and stepwise reactions on the ground state Tz PES, Pai et al. found that the lowest barrier to dissociation (∼3.5 eV) led to a symmetric concerted dissociation mechanism with the estimated barrier to a stepwise reaction slightly higher in energy (∼3.8 eV).[18] Using classical trajectory simulations on an interpolated ground state PES, Song et al. and Lee et al. found similar translational energy distributions to those measured by Gejo et al., but reinterpreted the results in light of a concerted mechanism with unequal distribution of available energy to the HCN products.[16,17] More recently, Dyakov et al. have employed ab initio and RRKM approaches to the dissociation of Tz and have explored several potential dissociation mechanisms arising from different locales on the ground state Tz PES, concluding that several mechanisms may occur from low-lying electronic excitations.[19] In regard to the work by Gejo et al., the study by Dyakov et al. also supports the notion that although the concerted mechanism may pass through a symmetric transition state, energy distribution to the HCN products may not be symmetric.

The present study marks one of only a handful of three-body coincidence experiments, and extrapolation of the detailed kinematics resulting from dissociation of Tz necessitated several advancements in the treatment and interpretation of data obtained from these types of measurements.[10] The primary impetus for this paper is to present in greater detail the experimental method that led to the conclusions made in refs 3 and 4. In particular, we present a thorough discussion of the dynamics associated with both the stepwise and symmetric concerted dissociation mechanisms observed upon CE of Tz^+ with Cs. The assignment of a stepwise mechanism upon excitation to the 3s Rydberg state of Tz was the result of an extensive Monte Carlo (MC) study on how stepwise mechanisms can manifest themselves in the data analysis techniques used in coincidence studies. Excitation into the $\pi^* \leftarrow$ n electronic manifold overlaps with the electronic excitation in previous photoexcitation experiments, and the strong evidence for a concerted breakup of Tz supports the conclusions made by recent theoretical studies on the dynamics proceeding from this region of the PES.

2. Experimental Section

The fast-beam translational spectrometer capable of coincidence detection of multiple neutral fragments has been previously described in detail and will be only briefly reviewed here.[24] Tz^+ was created by using an electrical discharge in a 1 kHz pulsed supersonic expansion (25 psig backing pressure) of a mixture of room temperature Tz (97%, Alfa Æsar) vapor (∼0.15 psi) seeded in 250 psig He at room temperature.[25] Cations were then skimmed, electrostatically accelerated to 12 or 16 keV, and rereferenced to ground potential by using a high-voltage switch. The cation of interest (*m*/*z* 81) was mass-selected by TOF and electrostatically guided through a ∼1 mm^3 interaction region in a collision cell containing $\sim 10^{-5}$ Torr Cs vapor. Unreacted cations were deflected out of the beam path and monitored by using a microchannel-plate-based detector. Neutral species formed in the collision cell were detected on a time- and position-sensitive neutral detector ∼110 cm from the collision cell.

The neutral detector consisted of a set of three 4 cm diameter microchannel plates in a *z*-stack arrangement above four adjacent crossed delay-line anodes.[26,27] Each individual anode in this array was capable of detecting the position and time of arrival for two particles given a 10 ns dead time, thus allowing detection of up to eight particles in coincidence for favorable recoil geometries. Given the cation beam energy, parent cation mass, and the time and position data for the recoiling fragments in each coincidence event, a full three-dimensional kinematic description of the dissociation process was obtained, including the fragment mass ratios, total kinetic energy release (KER), product recoil angles, and partitioning of momentum to each fragment.[24] The neutral detector was calibrated with the well-characterized 1.085 and 3.061 eV peaks in the KER spectrum for predissociation of the lowest Rydberg states of O_2 produced by CE of O_2^+ with Cs.[11]

A key requirement in the present experiment is the ability to produce Tz^+ that is stable on the time scale of the present experiment (>1 ms). Atomospheric pressure ionization mass spectrometry experiments have indeed detected Tz^+ after a drift time on the order of several milliseconds;[28] however, to our knowledge no experiments aimed at characterizing the structural or electronic properties of gas-phase Tz^+ have been reported in the literature. An adiabatic IP of 10.01 eV has been reported for production of ground state Tz^+, which is characterized by removal of an e′ electron from a primarily nonbonding orbital localized on a nitrogen atom (the *n*-type cation, $^2E'$).[29,30] Photoelectron spectra for Tz also show a second ionization limit at 11.69 eV, which is attributed to removal of an e″ electron from the aromatic π system (the π-type cation, $^2E''$).[29,30] Electron spin resonance spectroscopy experiments on Tz^+ in solution found that ionization of the neutral precursor with high-energy γ radiation produced only *n*-type cations.[31] Given no empirical evidence that our discharge ion source induces electronic excitation, we conduct further analysis under the assumption that only the *n*-type cation is being formed. By inference from previous spectroscopic characterization of the $^1E'$ 3s Rydberg state of Tz, the vibronic ground state of the *n*-type cation is expected to be on the lower sheet of a Jahn−Teller distorted (E ⊗ e) surface with minima at C_{2v} symmetry and below a conical intersection at D_{3h} symmetry.[32,33] The two-photon absorption experiments by Whetten et al. support the conclusion that the barrier to pseudorotation lies below the zero-point energy of the cation, yielding a fluxional ground state.[32−34]

3. Results

Although essential aspects of the three-body data obtained from CE of Tz^+ with Cs have been discussed previously,[3,4] new developments in the treatment of three-body coincidence data

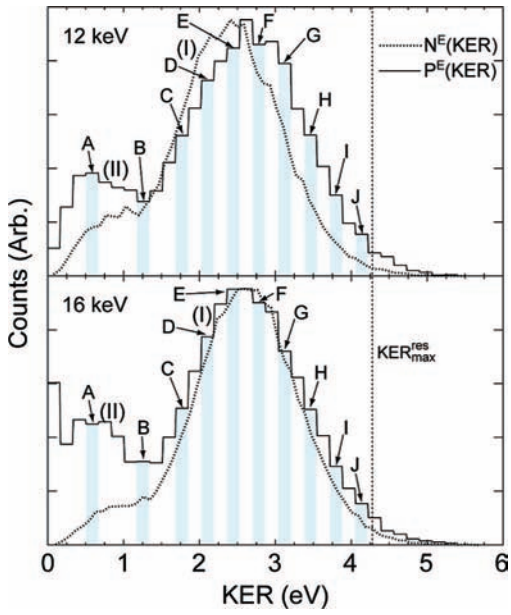

Figure 2. Measured N^E(KER) and corrected P^E(KER) distributions (in eV) for the three-body dissociation of 12 and 16 keV Tz^+ beams upon CE with Cs. The two primary features in the spectra are labeled as features I and II. A dotted line labeled KER^{res}_{max} at 4.26 eV marks the maximum allowed KER upon resonant excitation via CE. The labeled KER intervals are the following: A (0.51−0.68 eV), B (1.18−1.35 eV), C (1.69−1.86 eV), D (2.03−2.19 eV), E (2.36 −2.53 eV), F (2.70−2.87 eV), G (3.04−3.21 eV), H (3.38−3.54 eV), I (3.71−3.88 eV), and J (4.05−4.22 eV).

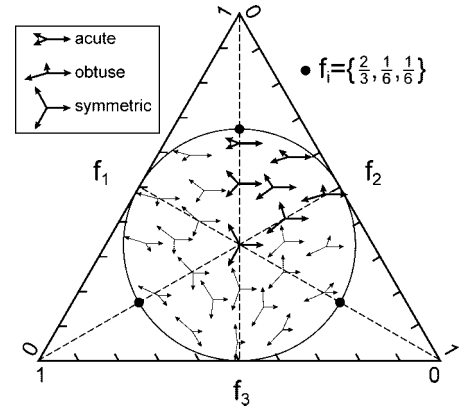

Figure 3. The Dalitz plot represented as a map of the momentum partitioned to three equal-mass fragments. Each axis of the Dalitz plot corresponds to the fractional square (f_i) of the momentum (p_i) imparted to one of the three fragments. For equal mass fragments, the equilateral triangle represents regions where energy is conserved and the inscribed circle represents the limits of the region where momentum is conserved. The dashed lines represent loci of C_{2v} symmetry in the product momentum partitioning. The acute apexes located at $f_i = \{^2/_3,^1/_6,^1/_6\}$ are indicated by black dots.

that have not been previously available in the literature will be addressed here in more detail. Two types of plots are used to display data collected in the present experiment: KER distributions are used to show the total measured KER for all three HCN products, and Dalitz representations[35] are used to illustrate momentum partitioning to the three products. Due to the finite size of the circular neutral particle detector, events with particular combinations of fragment momentum partitioning and laboratory-frame orientations were not able to be detected in coincidence. This can have a significant effect on the intensities of empirically measured distributions, causing them to differ from the true probability distributions that would be obtained from a detector with a full acceptance for all recoiling particles. A correction to KER distributions obtained from coincidence data that takes into account the finite size of the detector has been presented for the two-body case;[36] however, the analogous three-body correction is more complicated due to the complex kinematics associated with these types of processes. A similar correction for three-body Dalitz representations (described in the next section) employing MC simulations has been described previously,[37,38] although an extension of this correction to include three-body KER distributions is not available in the literature and will be presented in detail for the first time. On the basis of the historically proposed dissociation mechanisms for Tz, it is important to understand how stepwise and concerted processes appear in coincidence data. Previous investigations have shown that stepwise mechanisms produce characteristic (albeit subtle) features in the Dalitz plot,[39] and this was investigated by using MC simulations which will also be discussed.

Two different applications of MC simulations of the three-body dissociation processes in our experimental apparatus are presented in the following sections. To carry these out, a C++ code employing forward-convolution methods and a simple kinematic model of three-body reactions was used.[40] The geometric properties of the interaction region and scattering of neutral products resulting from neutralization of a fast cation beam with a defined energy and angular distribution, along with intrinsic properties of the neutral particle detector itself (e.g., size, dead-time, and dead areas) are accounted for in the simulation, which outputs time and position data that can be read into the same analysis code used for experimental data. Thorough treatments of the kinematics associated with concerted and stepwise three-body dissociation mechanisms have been presented previously, and were adhered to in the present MC simulations.[2,41,42]

3.1. Detector Acceptance Correction. On the basis of the raw time and position data obtained for recoiling fragments, empirical KER distributions, N^E(KER), were obtained for the three-body dissociative CE of Tz at 12 and 16 keV Tz^+ beam energies (shown as dotted traces in Figure 2). Both display a broad distribution from 0 to ∼5 eV and are devoid of fine structure, but exhibit two primary features peaked near 2.6 (feature I) and 0.5 eV (feature II). Because of the increased complexity in the kinematics associated with a three-body process when compared to the two-body case, the so-called detector acceptance function (DAF) correction of the N^E(KER) spectrum requires concomitant information about the dissociation dynamics. To illustrate the three-body dissociation dynamics in the present case, Dalitz representations were used.[35] The Dalitz plot is a two-dimensional histogram with three axes (yet only two independent variables) that correspond to the fractional square (f_i) of the momentum (p_i) imparted to each of the i fragments, as shown in eq 2:

$$f_i = \frac{|\vec{p}_i|^2}{\sum_i |\vec{p}_i|^2} \tag{2}$$

In short, single points on the Dalitz plot can be used to identify the magnitude and relative directions of the three momentum vectors obtained in a single three-body event (Figure 3).

To perform the correction, the experimental $N^E(KER)$ distributions are divided into n continuous equal-range KER intervals,

each denoted by Δ_j^{KER}. Each $N_j^E(\Delta_j^{KER})$ "bin" has a corresponding empirical Dalitz distribution for the measured events in that particular KER interval, represented by $\mathcal{N}_j^E(\Delta_j^{KER},f_1,f_2,1-f_1-f_2)$. MC simulations of the detector's geometric efficiency must be performed over each Δ_j^{KER} interval, inputting a constant probability for events to occur with any KER contained within Δ_j^{KER}. Fragment momentum partitioning in the simulation is sampled from an isotropic distribution within the circular region of the Dalitz plot where momentum is conserved. In the present experiment, no anisotropy was observed in the distribution of laboratory frame orientations of product recoil vectors so an isotropic distribution of laboratory frame orientations was sampled from the MC simulation. The resulting empirical Dalitz distributions from the simulation, $\mathcal{N}_j^{MC}(\Delta_j^{KER},f_1,f_2,1-f_1-f_2)$, can then be used to correct the $\mathcal{N}_j^E$ distributions over Δ_j^{KER} by using eq 3.

$$\mathcal{P}_j^E(\Delta_j^{KER},f_1,f_2,1-f_1-f_2) = \eta\cdot\frac{\mathcal{N}_j^E(\Delta_j^{KER},f_1,f_2,1-f_1-f_2)}{\mathcal{N}_j^{MC}(\Delta_j^{KER},f_1,f_2,1-f_1-f_2)} \quad (3)$$

Here, $\mathcal{P}_j^E$ is the DAF-corrected experimental Dalitz probability distribution over Δ_j^{KER}. A normalization factor (η) was included in eq 3 to account for the $\mathcal{N}_j^{MC}$ Dalitz distribution being an extensive quantity dependent on the number of iterations used in the MC simulation, and takes the value of the highest recorded intensity over all $\mathcal{N}_j^{MC}$ Dalitz distributions used in the correction process. This normalization scheme assumes that the same number of iterations are used per $\mathcal{N}_j^{MC}$ simulation and a 100% collection efficiency is obtained for a single bin in at least one of the n $\mathcal{N}_j^{MC}$ Dalitz distributions (which is within reason for events with low KER). The intensity of the corrected probability distribution at a given KER interval, $P_j^E(\Delta_j^{KER})$, can then be approximated by integrating $\mathcal{P}_j^E$ as shown in eq 4.

$$P_j^E(\Delta_j^{KER}) \approx \int_0^1\int_0^1 \mathcal{P}_j^E(\Delta_j^{KER},f_1,f_2,1-f_1-f_2)\,df_1\,df_2 \quad (4)$$

The binned $P^E(KER)$ distribution constructed using this method contains a single intensity for each KER interval and thus approaches the true continuous probability distribution in the limit where the number of intervals used approaches infinity.

The aforementioned correction cannot account for regions of the Dalitz plot where signal is not obtained in the experiment. For the case of the three-body dissociation of Tz the onset of geometrically undetectable events at a given beam energy is for dissociation with an equal partitioning of momentum among the three HCN fragments ($f_1 = f_2 = f_3 = 0.33$) and a high KER. Simple calculations and MC simulations showed that using an 11 keV cation beam results in a 100% loss of signal for a 5 eV KER in this case. Because of the kinematic simplicity of two-body experiments, data can be obtained at nearly any cation beam energy (typically between 6 and 16 keV) to exploit nonresonant CE effects—spectral features arising from different initial neutral states are qualitatively expected to show changing relative intensities as the beam energy is varied.[3−6] However, the present three-body experiment was limited to beam energies between 12 and 16 keV because of the full loss of signal in relevant regions of the Dalitz plot at lower beam energies. As discussed later, the change in relative velocity between the cation and Cs electron donor at these two beam energies yielded changes to the observed dissociation dynamics that were sufficient to aid the assignment of the initial excited states of Tz populated via the CE process.

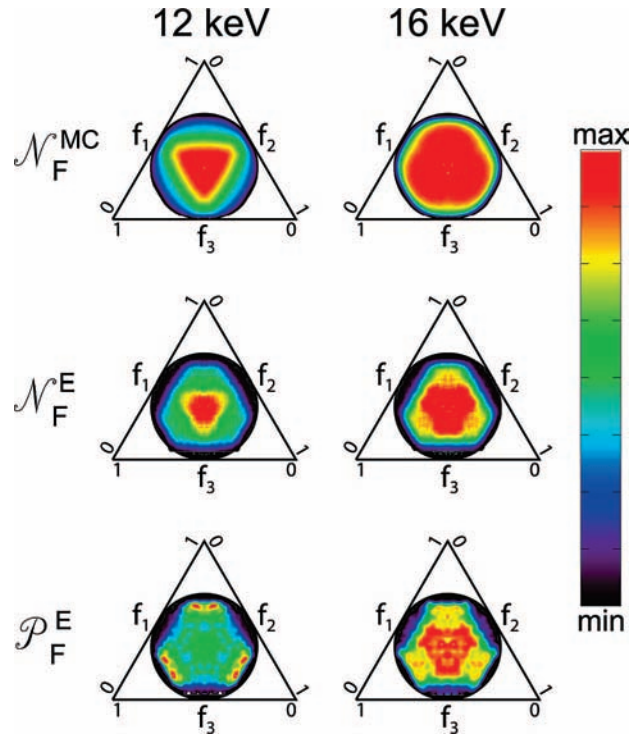

Figure 4. Example of the correction applied to Dalitz distributions over Δ_F^{KER} (2.70 to 2.87 eV) for data obtained with both 12 and 16 keV beams of Tz^+. The two upper plots depict $\mathcal{N}_F^{MC}$ distributions that result from MC simulations of the neutral particle detector's acceptance for an isotropic distribution in the momentum conserving circular region of the Dalitz plot. The two middle plots are the empirical experimentally measured $\mathcal{N}_F^E$ Dalitz distributions for three recoiling HCN products upon CE of Tz^+. The two bottom plots are the resulting $\mathcal{P}_F^E$ distributions after the correction described in Section 3.1 is applied.

The corrected $P^E(KER)$ distributions obtained upon CE of 12 and 16 keV cation beams are shown as solid histograms in Figure 2. $P^E(KER)$ distributions were constructed from the measured $N^E(KER)$ distributions by using $n = 32$ intervals over the KER range 0.0 to 5.4 eV and 2×10^6 events were used per MC simulation over each Δ_j^{KER} to ensure smooth $\mathcal{N}_j^{MC}$ Dalitz distributions. It is possible to increase the resolution of $P^E(KER)$ by increasing the number of intervals (n) used in the correction, although as a consequence the experimental Dalitz distributions suffer from lower signal-to-noise. In the present case, no fine structure was apparent in the $N^E(KER)$ distributions although small KER intervals were necessary to observe the KER-dependent changes in Dalitz distributions. It was iteratively concluded that using a value of $n = 32$ was sufficient to illustrate the relevant aspects of the experimental data while preserving favorable signal-to-noise in the final corrected experimental Dalitz distributions. An illustrative example of the Dalitz distributions used to convert empirical distributions to probability distributions over the KER interval labeled "F" in Figure 2 (Δ_F^{KER}; 2.70−2.87 eV) is presented in Figure 4.

Several of the corrected $\mathcal{P}_j^E$ Dalitz distributions obtained over different KER intervals (labeled A−J as indicated in Figure 2) are shown in Figure 5. As described previously, two distinct patterns appear in the Dalitz distributions over different KER ranges.[3,4] A feature with intensity primarily at the acute apexes of the Dalitz plot (where $f_i = \{^2/_3,^1/_6,^1/_6\}$ as indicated in Figure 3) is present between 1.5 and 5 eV, and a feature in the central

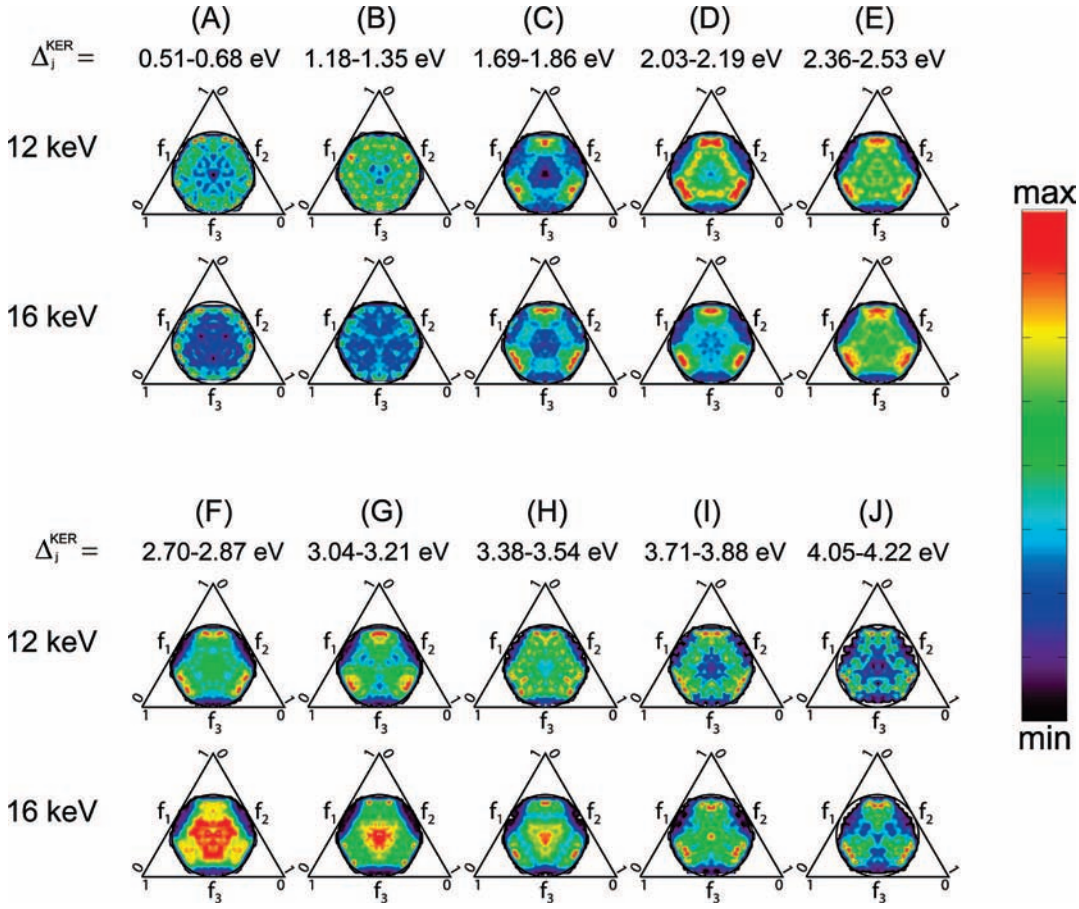

Figure 5. DAF corrected $\mathscr{P}_j^E$ Dalitz distributions from three-body dissociation of Tz upon CE of 12 and 16 keV Tz^+ beams with Cs. Each plot is constructed from events contained within the KER intervals (Δ_j^{KER}) labeled in Figure 2.

region corresponding to three symmetric momentum vectors occurs between 2 and 4 eV. Owing to the characteristic momentum partitioning in these features, they will respectively be referred to as the acute (i.e., two slow and one fast fragment) and symmetric (i.e., equal momentum partitioning) Dalitz features. The relative intensity of these features differs in the 12 and 16 keV data, qualitatively indicating that they arise from different initial excited states of neutral Tz. Qualitatively it is apparent that the acute mechanism is the dominant feature observed in the present experiment, although this could not be quantified due to the overlap of both features in Dalitz distributions. To clearly observe features of the symmetric mechanism, it was necessary to crop the most intense region of the acute mechanism (at the acute 2-fold symmetric apexes) in all experimental Dalitz distributions such that $f_i < 0.64$.

3.2. Monte Carlo Simulations of Stepwise Dissociation. To interpret the chemical dynamics that give rise to the acute Dalitz plot feature, an ad hoc Monte Carlo investigation into the effects of a stepwise dissociation mechanism on the Dalitz plot was employed. Because the Dalitz plot is constructed from final center-of-mass (c.m.) frame momentum vectors, it is straightforward to interpret in the case of a concerted dissociation mechanism—the correlated momentum vectors identify an instantaneous impulsive force driving the fragments apart. However, interpretation of the plot is not as intuitive in the case of a stepwise mechanism, which provided the primary motivation for the MC investigation. Although the Dalitz plots presented in Figure 5 are a convolution of both dissociation mechanisms, the plot obtained over Δ_C^{KER} (1.69 to 1.86 eV) at a 12 keV beam energy can be used to best illustrate the dynamics associated with the acute mechanism as it has little contribution from the symmetric mechanism.

A schematic representation of stepwise three-body dissociation of a three-particle system used in the MC simulation is illustrated in Figure 6. This mechanism is a two-step process with a separate two-body dissociation in each step. This simple model does not account for angular momentum conservation in the first step; partitioning of energy to rotational and vibrational degrees of freedom is accounted for in an ad hoc manner by choosing the kinetic energy (thus assuming the remaining available energy is partitioned to internal degrees of freedom). The total measured KER for the process (KER_{tot}) is defined as the sum of the KER occurring in each step, and a single factor (ε) can be used to describe this partitioning. A single factor α can also be used to describe the molecule's geometry for a stepwise dissociation; it is defined as the initial angle between the two bonds that serve as the axes for dissociation in each step. In the first dissociation step the "bound" $m_1m_2m_3$ molecule dissociates to $m_1 + m_2m_3 + \varepsilon \cdot KER_{tot}$ and linear-momentum-conserving velocity vectors $\vec{v}_1$ and $\vec{v}_{23}$ are associated with fragment m_1 and fragments m_2 and m_3, respectively (Figure 6a). In the second step the m_2m_3 intermediate is rotated counterclockwise through θ before dissociation to $m_2 + m_3 + (1 - \varepsilon) \cdot KER_{tot}$, and linear momentum-conserving velocity vectors $\vec{v}_2$ and $\vec{v}_3$ are obtained for fragments m_2 and m_3 (Figure 6b). The final c.m.-frame recoil velocity vectors ($\vec{v}_1^{lab}$,$\vec{v}_2^{lab}$,$\vec{v}_3^{lab}$) are then calculated by summation of the appropriate single-step velocity vectors for each fragment (Figure 6c,d).

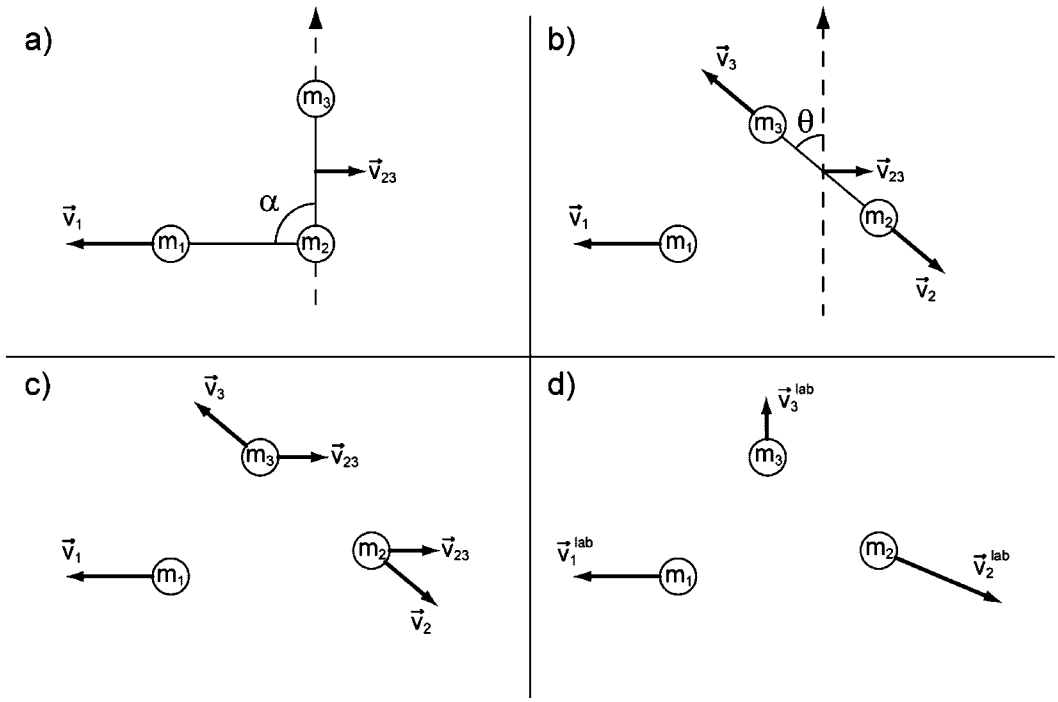

Figure 6. Schematic representation of a sequential three-body dissociation. Angle α is defined as the initial angle between the two bonds that serve as the axes for dissociation in each step. The molecule first dissociates to $m_1 + m_2m_3$ (a) followed by secondary dissociation of the m_2m_3 intermediate (b). Final laboratory frame recoil velocities are the sum of the velocities imparted on the fragments in the two dissociation processes (c, d).

Simulations were performed by using 10^6 iterations with an equal probability for KER_{tot} occurring between 1.69 and 1.86 eV (as mentioned previously, this was done to mirror the experimental Δ_C^{KER} interval even though the Dalitz plot does not have an inherent dependence on KER). To further mirror the experiment, Dalitz distributions obtained from MC simulations were subject to the aforementioned three-body DAF correction. Values for α, ε, and θ were sampled from Gaussian distributions with a mean (μ_k) and standard deviation (σ_k) associated with each distribution. The mass of each point mass in the simulation was fixed to be 27 au, and the α distribution was kept static with values of $\mu_\alpha = 90°$ and $\sigma_\alpha = 5°$. To simulate a true stepwise mechanism with no angular correlation between the two dissociation steps, sampling of θ was randomized, which consequently makes the choice of the input α distribution arbitrary. Laboratory frame orientations of the c.m.-frame recoil vectors were again randomly sampled from an isotropic distribution.

Several of the distinct patterns produced by varying μ_ε with $\sigma_\varepsilon = 0.01$ are displayed in Figure 7. All display a characteristic series of three lines that are parallel to the axes of the Dalitz plot, which result from the momentum vector associated with the first particle ($\vec{p}_1 = m_1 \cdot \vec{v}_1^{lab}$) being decoupled from the vectors associated with the two products formed in the second step of the stepwise mechanism ($\vec{p}_2 = m_2 \cdot \vec{v}_2^{lab}$ and $\vec{p}_3 = m_3 \cdot \vec{v}_3^{lab}$). In the case where three indistinguishable masses are used (i.e., $m_1 = m_2 = m_3$), the corresponding f_i values also become indistinguishable leading to a 3-fold symmetry in the plot. Simple vector addition from the kinematic model of stepwise dissociation presented in Figure 6 yields the result that dissociation of the first particle (m_1) will always lead to a static value of $f_1 = 2\varepsilon/3$ whereas the remaining two f_i values have a dependence on an angle ($\alpha - \theta$). Because θ is randomized in the present simulations, the origin of the linear feature can be quantitatively explained by the static value of f_1 (which is dependent on ε) while f_2 and f_3 are essentially random (although they are restrained by linear momentum conservation). Variation of σ_ε had no effect on the characteristic orientation of the linear features in the plot, although it made them more diffuse.

The Dalitz plot pattern produced from a stepwise mechanism with $\mu_\varepsilon = 0.25$ and $\sigma_\varepsilon = 0.15$ was found to be remarkably similar to the acute feature observed in the 12 keV plot over Δ_C^{KER}, which are shown in a side-by-side comparison in Figure 8. The similarity between the MC simulation and experimentally determined P_C^E distribution offers compelling evidence that the acute feature is the result of a sequential mechanism.

4. Discussion

The energy level diagram in Figure 1 shows the energy range over which each of the experimentally observed Dalitz plot features (i.e., the acute and symmetric features) are present relative to the ground state 3HCN dissociation limit. The labeled point at 4.26 eV above the 3HCN limit indicates the maximum KER if Tz was excited at resonance (also shown as a dotted line in Figure 2). This resonant energy is simply the difference in the ionization potentials of Tz (10.01 eV) and Cs (3.89 eV).[29] However, as has been shown in previous works the CE mechanism allows states lying energetically away from resonance to be populated, and this transition probability has a nonlinear dependence on the interaction time (and thus the beam velocity) between the cation and Cs.[3−6] The dissociation limit when one HCN fragment is produced in its lowest lying excited electronic state is endoergic with respect to resonant excitation of Tz by ∼2.2 eV and is not expected to be accessed in the present experiment.[43]

Evaluation of CE coupling strengths by using equation-of-motion coupled-cluster (EOM-CC) wave functions for a $(Cs-Tz)^+$ system in a generalized Mulliken-Hush approach has suggested that electronic states characterized by $R_s \leftarrow n$ and $\pi^* \leftarrow n$ transitions are the most likely initial states of Tz accessed in the present experiment.[3,4,44] Qualitatively, this is due to these states being the result of single electron transitions leaving a vacant lone-pair orbital, whereas excitation to

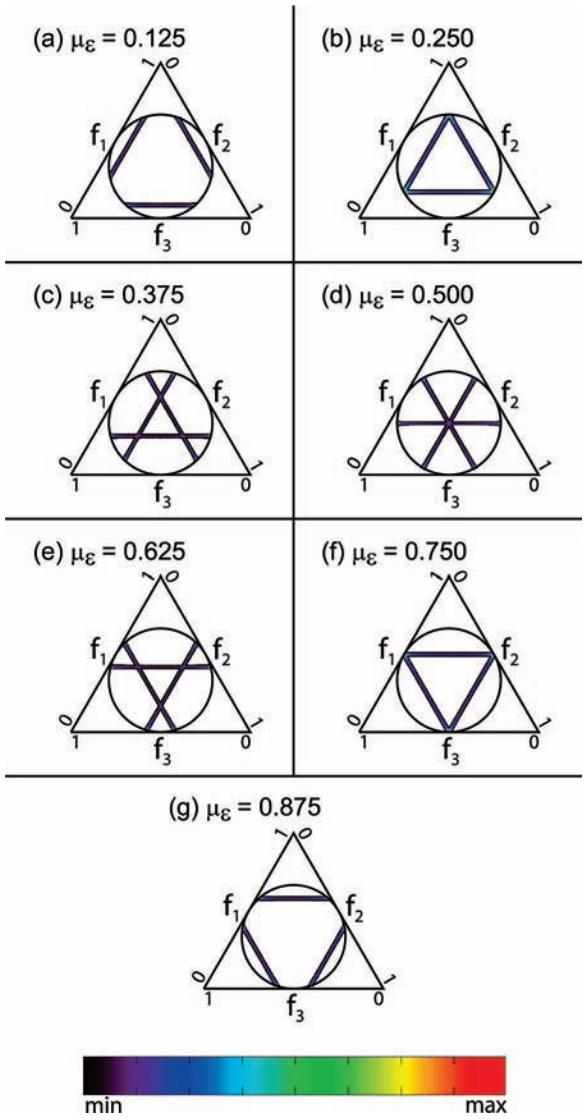

Figure 7. Characteristic Dalitz plot patterns resulting from MC simulations of the stepwise three-body dissociation of Tz for various values of μ_ε. The simulation was carried out for a 12 keV cation beam with a constant probability for the KER to occur anywhere over Δ_C^{KER}. Dalitz plots were DAF corrected by using the method outlined in the text. Other parameters used in the simulation were held at fixed values of $\sigma_\varepsilon = 0.01$, $\mu_\alpha = 90°$, and $\sigma_\alpha = 5°$.

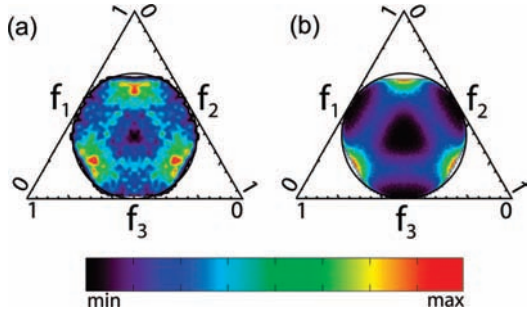

Figure 8. $\mathscr{P}_1^E$ Dalitz distributions from the three-body dissociation of Tz. (a) Experimental 12 keV $\mathscr{P}_C^E$ distribution ($\Delta_C^{KER} = 1.69-1.86$ eV). (b) $\mathscr{P}_C^E$ distribution arising from a MC simulation of a sequential dissociation process with $\mu_\alpha = 90°$, $\sigma_\alpha = 0°$, $\mu_\varepsilon = 0.25$, and $\sigma_\varepsilon = 0.15$.

$\pi^* \leftarrow \pi$ states would require significant rearrangement of the *n*-type cation core. On the basis of the maximum observed KER attributed to each Dalitz feature and high-level equation-of-motion ab initio calculations for electronically excited states (EOM-EE), our previous investigation was able to assign these initial excited electronic states of Tz to each distinct dissociation mechanism.[3,4] Symmetry correlation dictates that dissociation to three ground state HCN fragments must ultimately occur on the ground $^1A''_1$ electronic state of Tz[45] and it was shown that, in accordance with the reflection principle,[46] the dissociation dynamics reflect the topology of the initial excited state suggesting that dissociation proceeds rapidly on the ground state surface. Although the full mechanism through which an excited state of Tz produces 3HCN is likely to involve nonadiabatic interactions between multiple electronic states, the measured energetics and correlated product momenta provide insight toward the relationship between the initial stimulation of Tz and resulting dynamics in the products. The energetic and dynamical aspects of the two mechanisms will be discussed in the following sections.

4.1. Acute Mechanism. The acute dissociation mechanism has been assigned to initial excitation of Tz into the 3s Rydberg ($R_s \leftarrow n$) manifold. Previous EOM-EE calculations have predicted that the diabatic states comprising this manifold ($^3A_1$,$^1A_1$,$^3B_2$,$^1B_2$) lie between 5.11 ($^3A_1$) and 5.85 eV ($^1B_2$) above the 3HCN dissociation limit in the cation Franck−Condon (FC) region.[3,4] Because both singlet and triplet states are accessible in the present experiment, the energetics for both manifolds were considered and are included in the labeled region for this manifold in Figure 1. The calculated energetics for the singlet manifold are in reasonable agreement with vacuum ultraviolet studies reporting the origin of the vertical 3s $^1E' \leftarrow \tilde{X}^1A'_1$ transition at 6.92 eV (5.06 eV above the 3HCN limit), which marks an upper bound for the location of the vibronic ground state in the C_{2v} manifold.[47] As illustrated in Figure 1, the maximum observed KER where the acute feature occurs (~5 eV) is near the predicted energy for the lowest states contributing to this manifold in the cation FC region, and can be used to estimate the available energy for this product channel ($E_{avl} \approx 5$ eV).

The $R_s \leftarrow n$ manifold is comprised of two degenerate electronic states at D_{3h} symmetry, and the PES is characterized by the common E ⊗ e Jahn−Teller deformation ($E' \rightarrow A_1 + B_2$) with minima at C_{2v} symmetry and a conical intersection at D_{3h} symmetry (the so-called "Mexican hat"). In the lower vibronic regions of this surface, the equilibrated wave function will peak away from D_{3h} symmetry and the reflection principle prediction of an asymmetric partitioning of momentum from this initial state is observed in the experimental Dalitz distributions. Although both singlet and triplet manifolds are accessible via the CE mechanism, they lie close together and cannot be distinguished energetically in the present experiment. The topologies of singlet and triplet manifolds considered in this study were found to be similar, so in the case of the $R_s \leftarrow n$ manifold we describe the topology in terms of two states although there are potentially four accessible electronic states in this region of the PES. While the required coupling to the singlet ground state of Tz is conceivably more complicated starting from a triplet excited state, it cannot be ruled out. The degeneracies for triplet states actually make them statistically favored, although coupling rates to the ground state would be significantly smaller.

An aforementioned study by Goates et al. monitored the infrared emission from the ν_2 (bend) and ν_3 (C−H stretch) modes of HCN produced via 193 nm photolysis of neutral Tz (most likely inducing a $\pi^* \leftarrow \pi$ transition), and concluded that the internal energy carried away by HCN products was primarily

manifested as excitation of the bending mode of HCN.[21] In the absence of further information regarding the internal energy distribution in HCN products resulting from photoexcitation of Tz, we qualitatively assume that the majority of internal energy in the products produced in the present experiment (despite the differing mechanisms) will also be in the form of HCN bend excitation due to the strained conformation of HCN in the Tz ring structure. Because of the dominant nature of the acute mechanism, we estimate that the ⟨KER⟩ for events produced in this manner occurs near the 2.6 eV peak of feature I in the three-body P^{E}(KER) spectrum (Figure 2). The average internal energy carried away by the three HCN products can be estimated to be ∼2.4 eV, or 48% of E_{avl} for this product channel. Although this value is similar to those reported in other translational spectroscopy experiments,[14,15] it is not certain if any correlation is valid as all previous studies were most likely photoexciting Tz into the $\pi^* \leftarrow$ n and $\pi^* \leftarrow \pi$ electronic manifolds.

If the observed KER is indeed the result of a stepwise process (i.e., no angular correlation) similar to the predictions in the MC simulation, the iteratively determined KER partitioning parameter ($\varepsilon \approx 0.25$) suggests a primary KER of ∼0.7 eV and a secondary KER of ∼1.9 eV for events occurring with a total KER at the 2.6 eV peak in the P^{E}(KER) distributions. These results are markedly different than those of Gejo et al., who concluded they were observing a two-step process with angular correlation and a near-equal primary and secondary KER (i.e., $\varepsilon \approx 0.50$).

This KER partitioning has the surprising implication that an $(HCN)_2$ intermediate exists with greater than 1.9 eV of internal energy on a time scale larger than a rotational period. In their ab initio calculations on Tz decomposition, Pai et al. indicated a potential saddle point along the reaction coordinate corresponding to a cyclic diazete $(HCN)_2$ transition state;[18] however, spectra of stable $(HCN)_2$ in low-temperature Ar matrices have been assigned to a hydrogen-bonded structure similar to the dimer formed from "pure" HCN.[48,49] Previous translational spectroscopy experiments were not able to detect a long-lived HCN dimer, although on the time scale of the present experiment (<7 μs) a minor yet significant (∼25%) two-body channel was observed and will be discussed in the context of this work in a forthcoming paper.

4.2. Symmetric Mechanism. The symmetric mechanism was observed in Dalitz plots occurring with a KER between 2 and 4 eV and was previously concluded to be consistent with initial excitation into the upper states of the Tz $\pi^* \leftarrow$ n electronic manifold.[3,4] Because this mechanism was minor in comparison to the acute dissociation mechanism, its contribution to the P^{E}(KER) spectrum is difficult to separate and thus while the dynamics of this feature are readily observed, we are left with making primarily qualitative arguments regarding its energetics. The $\pi^* \leftarrow$ n manifold is comprised of four closely spaced states, two degenerate (E″) and two nondegenerate (A''_1, A''_2) under D_{3h} symmetry.[50] Similar to the case of the $R_s \leftarrow$ n manifold, although the topology of the $\pi^* \leftarrow$ n manifold is defined by the interaction of four states, when both singlets and triplets are considered there are actually eight accessible states in this region of the PES. The highest lying state in both the cation and neutral Tz FC regions, $^1E''$, has been predicted to consist of $^1A_2$ and $^1B_1$ diabats coupled through a glancing intersection at D_{3h} symmetry.[3,4] The two lower states in this manifold, A''_1 and A''_2, both exhibit PESs with minima away from D_{3h} symmetry and respectively correlate with A_2 and B_1 diabats in C_{2v} symmetry. Ab initio calculations predict that the states comprising this manifold lie extremely close together; in the C_{2v} FC region of the cation, the $^1A_2$ state (from $^1E''$) lies 3.67 eV above the 3HCN dissociation limit, with both the $^1B_1$ (from $^1E''$) and $^3A_2$ (from $^3A''_1$) diabats lying <0.25 eV lower in energy based on previous EOM-EE calculations.[3,4] Due to the ∼4 eV of available energy observed for this channel, it was concluded that the most likely initial state is population of one of these upper surfaces with minima at D_{3h} symmetry (see Figure 1).

The symmetric Dalitz feature is primarily comprised of events with near-symmetric partitioning of momentum among the products, but it also exhibits lobes pointing toward the 2-fold symmetric obtuse regions of the Dalitz plot (i.e., two fast and one slow fragment). Because the CE process is believed to be fast enough to result in a largely vertical transition to the neutral surface, it is within reason to expect excitation of asymmetric vibrational modes in a D_{3h} neutral PES as the transition is occurring from the fluxional C_{2v} Jahn−Teller distorted geometry of the cation. If the ensuing electronic transition to the ground state is sufficiently fast (i.e., no relaxation occurs in the excited state), it could potentially lead to asymmetries in the momentum partitioning as suggested by Dyakov et al. Another possible explanation for asymmetries in the symmetric Dalitz feature is that the wavepacket passes through a lower lying intermediate electronic state of lower symmetry before coupling to the ground state. Previous studies have indeed shown that the $\pi^* \leftarrow$ n states exhibit strong vibronic coupling, primarily along an in-plane symmetric ring-breathing mode.[51,52]

Although the $\pi^* \leftarrow$ n electronic manifold of Tz is believed to be accessed in both the present experiment and previous photoexcitation studies examining the photoinduced dissociation of Tz, due to the inherent differences between excitation of Tz via CE and excitation via photolysis it is unclear how observations made in the present experiment correlate with those made previously. In the most recent of these previous studies, Gejo et al. proposed a stepwise mechanism upon photoexcitation into the $\pi^* \leftarrow$ n and $\pi^* \leftarrow \pi$ electronic manifolds. This mechanism has been reinterpreted as an asymmetric concerted process in more recent theoretical investigations, and the asymmetries in the symmetric Dalitz feature in the present work favor the latter mechanism upon excitation into the $\pi^* \leftarrow$ n electronic manifold. Gejo et al. also found that the measured KER distribution did not vary significantly with the initial excited state (in stark contradiction to earlier work by Ondrey and Bersohn) thus favoring the exit channel defining the dissociation dynamics, whereas the present study clearly shows the initial formation of wavepacket on the ground state surface plays an important role in the underlying dynamics of Tz dissociation.

5. Conclusions

The present work provides a detailed description of the three-body data analysis and dynamics observed in the three-body dissociation of Tz upon CE of Tz^+ with Cs. This process induces both stepwise and nearly symmetric concerted dissociation mechanisms resulting from initial excitation into the $R_s \leftarrow$ n and $\pi^* \leftarrow$ n electronic manifolds, respectively. Studies employing ab inito, RRKM, and classical trajectory techniques have suggested that both mechanisms are possible and this marks the first direct observation of not just one but both pathways, which show a dependence on the initial state into which neutral Tz is excited.[16−19] The lack of a statistical redistribution of energy upon coupling to the ground state suggests that dissociation proceeds rapidly, making quantum dynamics simulations a suitable and potentially interesting theoretical choice to investigate nonadiabatic interactions on the Tz PES along with wavepacket propagation on the ground state surface.

Acknowledgment. This work was supported by the U.S. Air Force Office of Scientific Research under Grant No. FA9550-04-1-0035. The authors would like to thank A. I. Krylov and V. A. Mozhayskiy for their collaboration on the present work, as well as M. A. Fineman for his many contributions to this research.

References and Notes

(1) Thomas, R. D. *Mass Spectrom. Rev.* **2008**, *27*, 485.
(2) Maul, C.; Gericke, K. H. *Int. Rev. Phys. Chem.* **1997**, *16*, 1.
(3) Savee, J. D.; Mozhayskiy, V. A.; Mann, J. E.; Krylov, A. I.; Continetti, R. E. *Science* **2008**, *321*, 826.
(4) Mozhayskiy, V. A.; Savee, J. D.; Mann, J. E.; Continetti, R. E.; Krylov, A. I. *J. Phys. Chem. A* **2008**, *112*, 12345.
(5) Salop, A.; Lorents, D. C.; Peterson, J. R. *J. Chem. Phys.* **1971**, *54*, 1187.
(6) Sidis, V. *J. Phys. Chem.* **1989**, *93*, 8128.
(7) Laperle, C. M.; Mann, J. E.; Clements, T. G.; Continetti, R. E. *Phys. Rev. Lett.* **2004**, 93.
(8) Galster, U.; Baumgartner, F.; Muller, U.; Helm, H.; Jungen, M. *Phys. Rev. A* **2005**, 72.
(9) Mann, J. E.; Xie, Z.; Savee, J. D.; Braams, B. J.; Bowman, J. M.; Continetti, R. E. *J. Am. Chem. Soc.* **2008**, *130*, 3730.
(10) Continetti, R. E. *Annu. Rev. Phys. Chem.* **2001**, *52*, 165.
(11) Vanderzande, W. J.; Koot, W.; Peterson, J. R.; Los, J. *Chem. Phys. Lett.* **1987**, *140*, 175.
(12) Beijersbergen, J. H. M.; Dekoster, C. G.; Vanderzande, W. J.; Kistemaker, P. G.; Los, J. *Chem. Phys.* **1992**, *160*, 151.
(13) Beijersbergen, J. H. M.; Vanderzande, W. J.; Kistemaker, P. G.; Los, J.; Nibbering, N. M. M.; Nibbering, N. M. M. *J. Phys. Chem.* **1992**, *96*, 9288.
(14) Ondrey, G. S.; Bersohn, R. *J. Chem. Phys.* **1984**, *81*, 4517.
(15) Gejo, T.; Harrison, J. A.; Huber, J. R. *J. Phys. Chem.* **1996**, *100*, 13941.
(16) Song, K. Y.; Collins, M. A. *Chem. Phys. Lett.* **2001**, *335*, 481.
(17) Lee, J.; Dong, E. J.; Jin, D. S.; Song, K. Y.; Collins, M. A. *Phys. Chem. Chem. Phys.* **2004**, *6*, 945.
(18) Pai, S. V.; Chabalowski, C. F.; Rice, B. M. *J. Phys. Chem.* **1996**, *100*, 5681.
(19) Dyakov, Y. A.; Mebel, A. M.; Lin, S. H.; Lee, Y. T.; Ni, C. K. *J. Phys. Chem. A* **2007**, *111*, 9591.
(20) Innes, K. K.; Ross, I. G.; Moomaw, W. R. *J. Mol. Spectrosc.* **1988**, *132*, 492.
(21) Goates, S. R.; Chu, J. O.; Flynn, G. W. *J. Chem. Phys.* **1984**, *81*, 4521.
(22) Park, J. *Chem. Phys. Lett.* **1998**, *293*, 383.
(23) Kim, J. H.; Kim, H. L. *Chem. Phys. Lett.* **2001**, *333*, 45.
(24) Hanold, K. A.; Luong, A. K.; Clements, T. G.; Continetti, R. E. *Rev. Sci. Instrum.* **1999**, *70*, 2268.
(25) Bystrom, K. *J. Chem. Thermodyn.* **1982**, *14*, 865.
(26) Lampton, M.; Siegmund, O.; Raffanti, R. *Rev. Sci. Instrum.* **1987**, *58*, 2298.
(27) Friedman, P. G.; Cuza, R. A.; Fleischman, J. R.; Martin, C.; Schiminovich, D.; Doyle, D. J. *Rev. Sci. Instrum.* **1996**, *67*, 596.
(28) Kolaitis, L.; Lubman, D. M. *Anal. Chem.* **1986**, *58*, 1993.
(29) Fridh, C.; Asbrink, L.; Jonsson, B. O.; Lindholm, E. *Int. J. Mass Spectrom. Ion Phys.* **1972**, *8*, 85.
(30) Gleiter, R.; Hornung, V.; Heilbron, E. *Helv. Chim. Acta* **1972**, *55*, 255.
(31) Rhodes, C. J. *J. Chem. Res., Synop.* **1989**, 76.
(32) Whetten, R. L.; Grant, E. R. *J. Chem. Phys.* **1984**, *81*, 691.
(33) Whetten, R. L.; Haber, K. S.; Grant, E. R. *J. Chem. Phys.* **1986**, *84*, 1270.
(34) Kato, H.; Hirao, K.; Yamashita, K. *THEOCHEM* **1982**, *5*, 265.
(35) Dalitz, R. H. *Philos. Mag.* **1953**, *44*, 1068.
(36) Continetti, R. E.; Cyr, D. R.; Osborn, D. L.; Leahy, D. J.; Neumark, D. M. *J. Chem. Phys.* **1993**, *99*, 2616.
(37) Galster, U.; Kaminski, P.; Beckert, M.; Helm, H.; Muller, U. *Eur. Phys. J. D* **2001**, *17*, 307.
(38) Strasser, D.; Lammich, L.; Kreckel, H.; Krohn, S.; Lange, M.; Naaman, A.; Schwalm, D.; Wolf, A.; Zajfman, D. *Phys. Rev. A* **2002**, *66*, 032719.
(39) Matsuda, A.; Fushitani, M.; Thomas, R. D.; Zhaunerchyk, V.; Hishikawa, A. *J. Phys. Chem. A*, DOI: 10.1021/jp806466x.
(40) Clements, T. G. Ph. D. Thesis, University of California at San Diego, 2002.
(41) Maul, C.; Gericke, K. H. *J. Phys. Chem. A* **2000**, *104*, 2531.
(42) Hishikawa, A.; Hasegawa, H.; Yamanouchi, K. *Chem. Phys. Lett.* **2002**, *361*, 245.
(43) Herzberg, G. *Molecular Spectra and Molecular Structure III. Electronic Spectra of Polyatomic Molecules*; D. van Nostrand Company, Inc.: Princeton, NJ, 1966.
(44) Cave, R. J.; Newton, M. D. *Chem. Phys. Lett.* **1996**, *249*, 15.
(45) Osamura, Y.; Unno, M.; Hashimoto, K. *J. Am. Chem. Soc.* **1987**, *109*, 1370.
(46) Schinke, R. *Photodissociation Dynamics*; Cambridge University Press: Cambridge, UK, 1993.
(47) Walker, I. C.; Palmer, M. H.; Ballard, C. C. *Chem. Phys.* **1992**, *167*, 61.
(48) King, C. M.; Nixon, E. R. *J. Chem. Phys.* **1968**, *48*, 1685.
(49) Satoshi, K.; Takayanagi, M.; Nakata, M. *J. Mol. Struct.* **1997**, *413*, 365.
(50) Bolovinos, A.; Tsekeris, P.; Philis, J.; Pantos, E.; Andritsopoulos, G. *J. Mol. Spectrosc.* **1984**, *103*, 240.
(51) Webb, J. D.; Swift, K. M.; Bernstein, E. R. *J. Chem. Phys.* **1980**, *73*, 4891.
(52) Fischer, G.; Katz, B. *Chem. Phys. Lett.* **1983**, *96*, 47.

JP810365F